

Dust attenuation evolution in $z \sim 2 - 12$ JWST galaxies

Vladan Markov^{1,*}, Simona Gallerani¹, Andrea Ferrara¹, Andrea Pallottini¹, Eleonora Parlanti¹, Fabio Di Mascia¹, Laura Sommovigo², and Mahsa Kohandel¹

¹Scuola Normale Superiore, Piazza dei Cavalieri 7, 56126 Pisa, Italy

²Center for Computational Astrophysics, Flatiron Institute, 162 5th Avenue, New York, NY 10010, USA

*vladan.markov@sns.it

A sizable fraction of the heavy elements synthesized by stars in galaxies condenses into sub-micron-sized solid-state particles, known as dust grains^{1,2}. Dust produces a wavelength-dependent attenuation, A_λ , of the galaxy emission, thereby significantly altering its observed properties³. Locally, A_λ is in general the sum of a power-law and a UV feature ('bump')⁴ produced by small, carbon-based grains⁵. However, scant information exists regarding its evolution across cosmic time. Here, leveraging data from 173 galaxies observed by the James Webb Space Telescope in the redshift range $z = 2 - 12$ ⁶, we report the most distant detection of the UV bump in a $z \sim 7.55$ galaxy (when the Universe was only ~ 700 Myr old), and show for the first time that the power-law slope and the bump strength decrease towards high redshifts. We propose that the flat A_λ shape at early epochs is produced by large grains newly formed in supernova ejecta⁷, which act as the main dust factories at such early epochs. Importantly, these grains have undergone minimal reprocessing in the interstellar medium due to the limited available cosmic time⁸. This discovery opens new perspectives in the study of cosmic dust origin and evolution.

Introduction

Dust attenuation refers to the absorption and scattering of photons along the line of sight (LOS), due to the intervening interstellar medium (ISM) dust. The shape of the dust attenuation curve, A_λ , in galaxies (i.e. the slope of the curve and the strength of the characteristic UV bump at ~ 2175 Å) is determined by both the intrinsic dust properties (mass, grain size distribution, chemical composition), and the spatial distribution of dust with respect to stars. In the case of simple dust-to-star geometry, e.g., a point-like background source with a uniform dust screen, the loss of light along the LOS is instead referred to as "dust extinction", which is governed solely by the intrinsic dust properties^{4,9}.

The slope of the attenuation curve is determined by the grain size distribution and chemical composition^{1,5,10}. In particular, a shift towards smaller (larger) grains results in steeper (shallower) shapes⁵. Likewise, the rise of the characteristic UV bump feature at 2175 Å is typically associated with the existence of small carbonaceous dust grains^{10,11}, including polycyclic aromatic hydrocarbons (PAHs)^{12,13}. The V-band attenuation, A_V , which serves as a proxy of the galaxy dust content along the LOS, has been identified as one of the primary drivers of the shape of the dust attenuation law^{14,15}. Theoretical studies suggest that this correlation may arise from radiative transfer effects in galaxies where dust has a complex distribution relative to different stellar populations^{16,17}. For instance, the increasing complexity of the dust-to-star geometry flattens the slope of the dust attenuation curve and reduces the prominence of the UV bump, regardless of the initial dust extinction curve^{16,18}.

The dust attenuation/extinction laws of high- z sources remain largely unknown. Only a handful of early star-forming galaxies¹⁹⁻²¹, quasars^{22,23}, and gamma-ray burst (GRB) afterglows^{24,25} have constrained dust curves. Dust laws at high- z are expected to deviate from the well-established empirical dust curves of the local galaxies, such as the "Calzetti"²⁶ attenuation curve for local starbursts, and the Small Magellanic Cloud (SMC)²⁷ and the Milky Way (MW) extinction curves²⁸. This redshift (z) evolution may arise from several factors such as distinct dust formation processes^{29,30}, and dust reprocessing mechanisms^{31,32} occurring in the more extreme ISM conditions³³⁻³⁷ of early galaxies. Additionally, galaxies at intermediate^{38,39} and high- z ^{40,41} tend to be less dusty and show a clumpier structure and irregular distribution of dust and gas with respect to stars, compared to nearby sources⁴²⁻⁴⁵.

In this Letter, we apply our customized version of the BAGPIPES code^{20,46} to a large sample of star-forming galaxies at $z \sim 2 - 12$, from the publicly available *James Webb* Space Telescope (JWST) spectroscopic observations, to investigate evolutionary trends of dust attenuation laws and their implications on the intrinsic dust properties and dust-to-star geometry.

Redshift evolution of dust attenuation law

We employ our customized version of BAGPIPES code²⁰ to fit the individual spectra of a sample of 173 JWST galaxies at $z \sim 2 - 12$. The code generates the best-fit model to the NIRSpec spectra and provides the best-fit parameters of the SED model from the medians of the posterior distribution. Outputs of the SED fitting process include fundamental physical characteristics of galaxies (stellar mass, star formation rate (SFR), metallicity, stellar age, ionization parameter, and V-band dust attenuation

A_V) along with the properties of the dust attenuation model ($c_1 - c_4$; see the SED fitting section for details). We utilize the $c_1 - c_4$ parameters to construct the dust attenuation curve for each galaxy. The inferred attenuation curves of our sample exhibit a wide diversity of slopes and UV bump strengths (see Fig. 3 and the Galaxy Sample section). To explore potential trends in dust attenuation evolution, we split our sample in redshift bins by adopting equidistant cosmic time in each bin ($\Delta t \sim 0.5$ Gyr). The number of sources per bin varies in the 13-66 range.

Fig. 1 depicts the median dust curves with the corresponding 1σ uncertainties for each subsample. Although the associated uncertainties are relatively large, a noticeable trend emerges in the evolution of the dust attenuation curves with redshift. Specifically, with increasing redshift, the median slope flattens and the strength of the UV bump decreases.

To provide a more quantitative analysis of these results, we characterize the shape of the dust attenuation curve with the S and B parameters, which represent proxies for the UV-optical slope and the 2175 Å bump strength, respectively⁴. The slope is defined by the ratio of attenuation at 1500 Å and the one in the V -band, $S = A_{1500}/A_V$. The UV bump strength is defined as $B = A_{\text{bump}}/A_{2175}$, where A_{bump} is the additional attenuation above the baseline at 2175 Å, and A_{2175} is the total attenuation at 2175 Å (see the Attenuation curve parametrization section). The trends that we see in Fig. 1 remain apparent when we plot the UV-optical dust curve slope (S) and UV bump strength (B) separately, as functions of redshift (Figs. 2a and 2b, respectively).

Redshift evolution of the slope

Fig. 2a illustrates the redshift evolution of the UV-optical slope (S), for each source of our full JWST sample, and for subsamples grouped by redshift (as in Fig. 1). The median slope of $z \sim 2 - 3.5$ JWST galaxies approaches the SMC slope²⁷. However, it gradually flattens with increasing redshift ($z \sim 3.5 - 5.5$) and at $z > 5.5$ for JWST galaxies is flatter than the MW slope²⁸. The median slopes of JWST galaxies at intermediate- z are slightly steeper (although they are consistent within the 1σ uncertainties) with respect to most of the inferred slopes of various samples of nearby and intermediate- z galaxies from the literature. The discrepancy can be attributed to the fact that our overall JWST sample has a median A_V of ~ 0.38 . Conversely, the values of A_V for most galaxy samples in the literature are somewhat higher, $A_V \sim 0.4 - 1.0$ ²⁶, $A_V \sim 0.9$ ⁴⁷, $A_V \gtrsim 0.5$ ⁴⁸⁻⁵¹, $A_V \sim 0.2 - 1.1$ ⁵², and $A_V \sim 0.3 - 0.9$ ⁵³. Therefore, this difference in slopes is a consequence of a well-known trend wherein galaxies with low A_V tend to have steeper UV-optical slopes^{14, 16, 19}. If we instead restrict our JWST sample to more attenuated galaxies (with $A_V > 0.38$), our results are more aligned with the slopes inferred for known samples of $z \sim 0 - 3$ galaxies. We discuss the potential origin of this discrepancy in the Observational and model uncertainties section.

Fig. 2a also shows that the slope of the attenuation curve (at fixed redshift) flattens with increasing A_V , as expected. This effect is more evident at lower redshifts ($z \lesssim 4$), whereas at $z \gtrsim 6$ the dust attenuation curves remain shallow, and are largely unaffected by variations in A_V . Furthermore, the analysis of $A_\lambda(z)$ in different A_V ranges shows that the flattening trend towards high- z persists irrespective of the A_V values considered. This implies that A_V is not the driver of the redshift evolution of the slope. Additionally, we examine if the flattening trend stems from an underlying dependence on other galaxy properties, but the overall trends remain regardless of the considered values.

Redshift evolution of the UV bump strength

Fig. 2b depicts the redshift evolution of the UV bump strength (B). Similarly to the observed trends with the slope S , B also exhibits a general decrease as redshift increases. The median B value reaches levels comparable to $\sim 30\%$ of the MW bump strength in the $z \sim 2 - 4$ range. This is comparable with the inferred B values of the intermediate- z galaxies found in the literature^{47, 49}, although the uncertainties remain relatively high. To further support this result, we emphasize that if we characterize the UV bump strength using the c_4 parameter (Eq. 1⁵⁴), we observe comparable trends in the redshift evolution of the UV bump strength (Fig. 4).

The presence of the UV bump has been confirmed with a significance level of $\sigma > 3$, for 28 sources, within the $z \sim 2 - 8$ range (marked by red open circles in Fig. 2b). This accounts for $\sim 16\%$ of the full JWST sample. However, B is not well constrained and exhibits high uncertainties due to error propagation. If instead we use the c_4 parameter, which is better constrained as an output of the SED fitting procedure, we obtain a securely detected UV bump in $\sim 21\%$ of the sources (red open circles in Fig. 4). This percentage ($\sim 21\%$) is consistent with previous results^{48, 55} found in samples of $z \sim 1.0 - 2.5$ galaxies. The median bump strength of sources with UV bump detection is $B \approx 0.7 \times B^{\text{MW}}$, i.e., $c_4 \approx 0.75 \times c_4^{\text{MW}}$.

Applying both B and c_4 parameterizations, we confirm that the highest redshift galaxy of our JWST sample with a reliable UV bump detection is the 1433_3989 source at $z \sim 6.14$ (Fig. 5a-c). The UV bump strength for 1433_3989 is measured as $B = 0.43 \pm 0.05$ ($\sigma > 9$) or $c_4 = 0.083 \pm 0.014$ ($\sigma > 6$), which corresponds to a factor of ~ 1.2 or ~ 1.6 higher than the MW bump, depending on the considered parametrization. Moreover, the highest redshift source with a confirmed UV bump detection using only the B parameter is the 2750_449 source at $z \sim 7.55$ (Fig. 5d-f). The UV bump strength for 2750_449 is quantified as $B = 0.34 \pm 0.1$ ($\sigma > 3$) or $c_4 = 0.054 \pm 0.025$ ($\sigma > 2$) (i.e., ~ 0.95 or ~ 1.05 of the MW bump).

Discussion

Our results show that the attenuation law evolves with redshift. Specifically, the attenuation slope flattens (from $S > 4$ at $z \sim 2$ to $S \sim 2$ at $z > 8$) at high- z . This trend is found independently of the value of A_V . Furthermore, the strength of the UV bump decreases and eventually disappears (from $B \sim 0.1$ at $z \sim 2$ to $B \sim 0$ at $z > 5.5$) at early epochs.

We now turn to the interpretation of these findings. In principle, the observed evolutionary trends can be explained by three scenarios: radiative transfer (RT) effects dependent on (1) the amount of attenuation, i.e. A_V , or (2) dust distribution relative to stars of various ages, or (3) changes in the intrinsic dust properties (primarily grain size distribution and chemical composition). Although in general identifying the dominant factor is challenging³, the quality of the present data allows us to draw solid conclusions.

It is well established that smaller (larger) A_V values produce steeper (flatter) attenuation curves. Such correlation has been both predicted^{14,16,17} and observed^{4,56}. The physical interpretation is that, in the low- A_V (optically thin) limit, UV photons have a higher probability of being scattered and eventually absorbed, leading to the steepening of the slope^{14,57}. In the high- A_V (optically thick) limit, the shape of the curve is flattened by both scattering into the LOS and radiation from unobscured OB stars¹⁶. Indeed, we also find (Fig. 2a) that *at fixed redshift* S increases with decreasing A_V . However, we do see that the flattening trend towards high- z persists irrespective of A_V . We can then rule out the first scenario.

Scenario (2) is based on the evidence that complex dust-to-star geometries flatten the slopes and reduce the UV bump strengths of dust attenuation curves^{16–18,58} as in those conditions UV photons from young stars escape more easily. Although the distribution of dust and gas in galaxies is often not easy to measure, a similar clumpier ISM structure is reported in both intermediate- and high- z galaxies compared to more local sources^{42,43,59}. This suggests that the evolution of the geometry, and hence of the attenuation curve, in the considered $z \sim 2 - 11.5$ range should be rather modest. Thus, scenario (2) seems unlikely.

Scenario (3) invokes changes in the grain properties. First, we note that our results are consistent with predictions from theoretical studies^{60–62} that have investigated the cosmological evolution of interstellar dust. A recent study⁶² finds that, at a fixed metallicity, extinction curves flatten and the UV bump becomes less prominent with redshift. The study concluded that such trends are driven by a shift in the grain size distribution, favouring larger grains at early epochs. What causes such a shift?

The early prevalence of large grains could be attributed to dust production mechanisms in the ejecta of core-collapse Type II supernovae (SNII^{7,63}). These dust sources are predicted to predominantly form large ($\approx 0.1 \mu\text{m}$) grains^{8,60,63}. Grains are then released into the ISM where they undergo shattering processes^{60–62,64} breaking them into smaller units. However, shattering is a rather slow process, with typical timescales of $\gtrsim 0.5 - 1 \text{ Gyr}$ ^{8,60}. As a consequence, the transition from large to smaller grains is very gradual and is completed only by $z \approx 6$. Alternatively, small grains might be preferentially destroyed by Coulomb explosions in the presence of strong radiation fields^{65,66} as the ones present in early, compact galaxies.

The redshift evolution of S and B (or c_4) we find supports the third scenario. Importantly, the slope remains consistently shallow with a small dispersion at $z \gtrsim 5.5$. This might be interpreted with the existence of a single, dominant dust formation channel (i.e. SNII), in which large grains are formed and only minimally reprocessed in the ISM in the limited cosmic time available. The decrease of the bump strength towards high- z also supports this interpretation, as SNII yields ($\sim 90\%$ of silicate and $\sim 10\%$ of carbon dust) are scarce of carbonaceous grains⁶¹.

At $z \lesssim 5 - 5.5$, a larger variety of attenuation curves is observed. This is likely due to a combination of several effects, including the transition from SNII to asymptotic giant branch (AGB) stars^{67,68} as the dominant dust sources, dust growth in the ISM^{8,69}, more efficient shattering and sputtering^{60–62,64}. Concurrently, the UV bump emerges at $z \lesssim 5$ (around $\sim 1.2 \text{ Gyr}$), marking the epoch when dust formation in AGB stars becomes dominant, leading to enhanced production of carbonaceous grains. Finally, a marginal decrease in both S and B at $z \lesssim 3.4$ may be attributed to processes such as coagulation and accretion becoming more prominent at later epochs^{61,64}.

In summary, the flattening of dust attenuation curves at high- z suggests that we might be observing galaxies through a curtain of dust newly formed in SNII ejecta, although other less likely explanations cannot be completely excluded. Progress might come from cosmological hydrodynamic simulations including dust and related RT effects^{23,42}. These will make it possible to accurately determine the dust-to-star geometry, incorporate and explore different intrinsic dust properties (grain size distribution and chemical composition), and take into account RT effects. In parallel, insights into the intrinsic dust properties of high- z sources can be gained via observations of point-like sources, such as quasars^{22,70}, and gamma-ray burst afterglows^{24,25}.

References

1. Mathis, J. S., Rumpl, W. & Nordsieck, K. H. The size distribution of interstellar grains. *ApJ* **217**, 425–433, DOI: [10.1086/155591](https://doi.org/10.1086/155591) (1977).
2. Draine, B. T. Interstellar Dust Grains. *ARA@AND@A* **41**, 241–289, DOI: [10.1146/annurev.astro.41.011802.094840](https://doi.org/10.1146/annurev.astro.41.011802.094840) (2003). [astro-ph/0304489](https://doi.org/10.1146/annurev.astro.41.011802.094840).

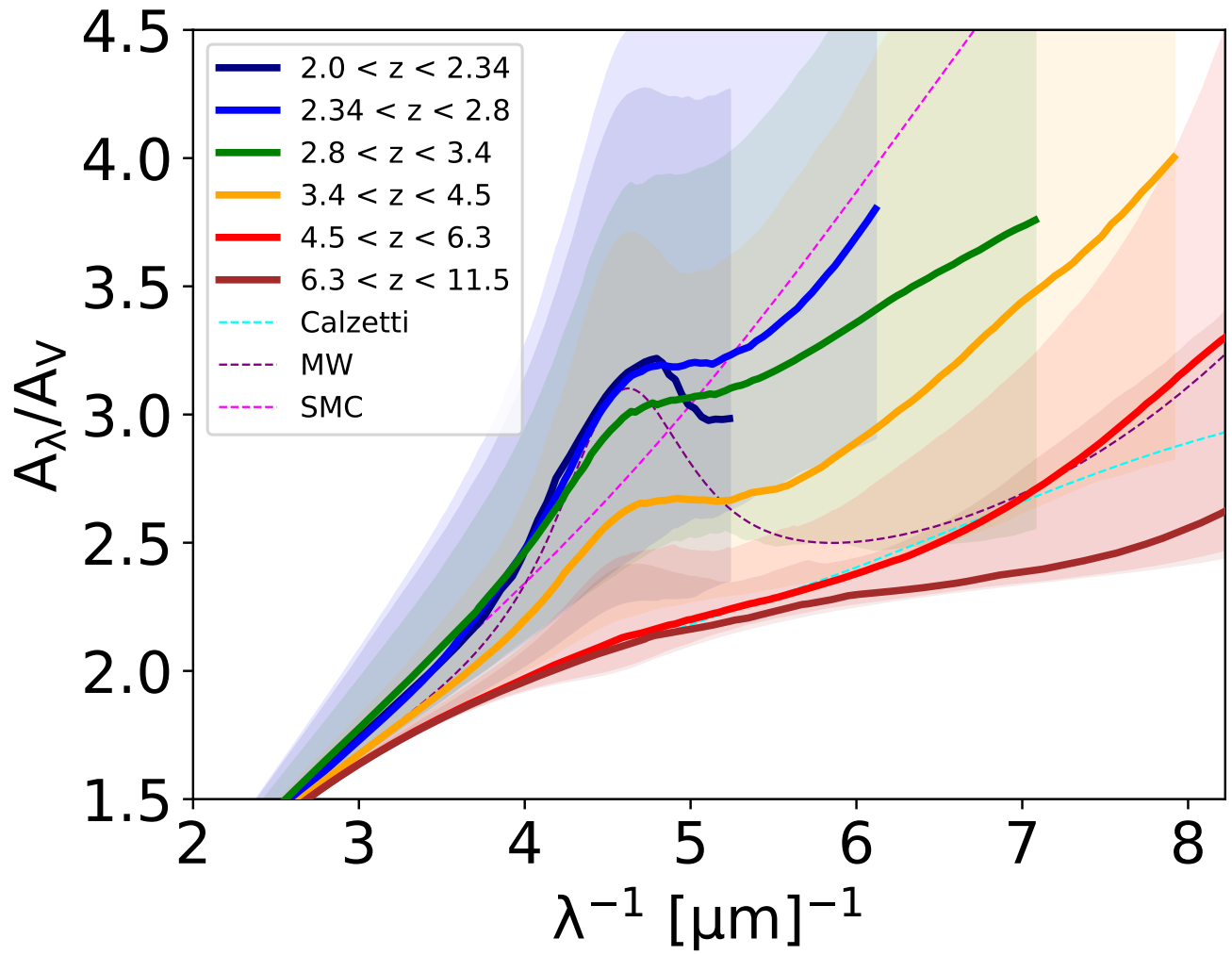


Figure 1. Dust attenuation curves of our full sample of $z \sim 2 - 12$ JWST galaxies binned by redshift. The Calzetti, the MW, and the SMC empirical curves are shown as cyan, purple and magenta dashed lines, respectively.

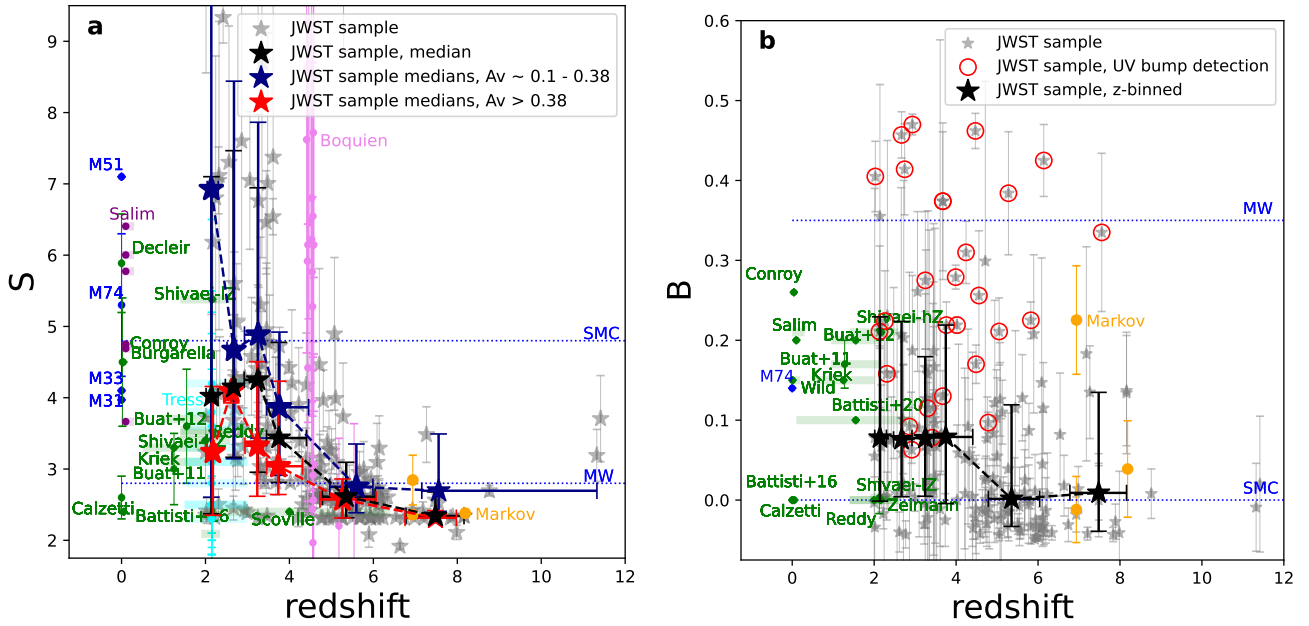


Figure 2. Dust attenuation parameters as a function of redshift. a, UV-optical slope (S) as a function of redshift. Our JWST galaxy sample is represented by grey stars. The median slopes and bump strengths of galaxies binned by redshift (corresponding to the redshift bins of Fig. 1) are indicated by black stars. Sources with $A_V \sim 0.1 - 0.38$ (86 sources) and $A_V > 0.38$ (87), represented by navy blue and red stars, respectively. Literature results are depicted as coloured circles (See the Comparison with the literature section). Corresponding horizontal stripes indicate the redshift range of galaxies for which the median/mean parameters have been estimated. **b**, UV bump strength (B) as a function of redshift. JWST sources with UV bump detection are highlighted by a red circle.

3. Conroy, C. Modeling the Panchromatic Spectral Energy Distributions of Galaxies. *ARA@AND@A* **51**, 393–455, DOI: [10.1146/annurev-astro-082812-141017](https://doi.org/10.1146/annurev-astro-082812-141017) (2013). [1301.7095](https://arxiv.org/abs/1301.7095).
4. Salim, S. & Narayanan, D. The Dust Attenuation Law in Galaxies. *ARA@AND@A* **58**, 529–575, DOI: [10.1146/annurev-astro-032620-021933](https://doi.org/10.1146/annurev-astro-032620-021933) (2020). [2001.03181](https://arxiv.org/abs/2001.03181).
5. Weingartner, J. C. & Draine, B. T. Dust Grain-Size Distributions and Extinction in the Milky Way, Large Magellanic Cloud, and Small Magellanic Cloud. *ApJ* **548**, 296–309, DOI: [10.1086/318651](https://doi.org/10.1086/318651) (2001). [astro-ph/0008146](https://arxiv.org/abs/astro-ph/0008146).
6. Brammer, G. Dawn jwst archive. <https://dawn-cph.github.io/dja/index.html> (2023).
7. Todini, P. & Ferrara, A. Dust formation in primordial Type II supernovae. *MNRAS* **325**, 726–736, DOI: [10.1046/j.1365-8711.2001.04486.x](https://doi.org/10.1046/j.1365-8711.2001.04486.x) (2001). [astro-ph/0009176](https://arxiv.org/abs/astro-ph/0009176).
8. Asano, R. S., Takeuchi, T. T., Hirashita, H. & Inoue, A. K. Dust formation history of galaxies: A critical role of metallicity for the dust mass growth by accreting materials in the interstellar medium. *Earth, Planets Space* **65**, 213–222, DOI: [10.5047/eps.2012.04.014](https://doi.org/10.5047/eps.2012.04.014) (2013). [1206.0817](https://arxiv.org/abs/1206.0817).
9. Calzetti, D. Star Formation Rate Indicators. In Falcón-Barroso, J. & Knapen, J. H. (eds.) *Secular Evolution of Galaxies*, 419, DOI: [10.48550/arXiv.1208.2997](https://doi.org/10.48550/arXiv.1208.2997) (2013).
10. Draine, B. T. & Lee, H. M. Optical Properties of Interstellar Graphite and Silicate Grains. *ApJ* **285**, 89, DOI: [10.1086/162480](https://doi.org/10.1086/162480) (1984).
11. Stecher, T. P. Interstellar Extinction in the Ultraviolet. *ApJ* **142**, 1683, DOI: [10.1086/148462](https://doi.org/10.1086/148462) (1965).
12. Desert, F. X., Boulanger, F. & Puget, J. L. Interstellar Dust Models for Extinction and Emission. *A@AND@A* **237**, 215 (1990).
13. Siebenmorgen, R. & Kruegel, E. Dust model containing polycyclic aromatic hydrocarbons in various environments. *A@AND@A* **259**, 614–626 (1992).
14. Chevillard, J., Charlot, S., Wandelt, B. & Wild, V. Insights into the content and spatial distribution of dust from the integrated spectral properties of galaxies. *MNRAS* **432**, 2061–2091, DOI: [10.1093/mnras/stt523](https://doi.org/10.1093/mnras/stt523) (2013). [1303.6631](https://arxiv.org/abs/1303.6631).
15. Battisti, A. J., Cunha, E. d., Shivaei, I. & Calzetti, D. The Strength of the 2175 Å Feature in the Attenuation Curves of Galaxies at $0.1 < z \lesssim 3$. *ApJ* **888**, 108, DOI: [10.3847/1538-4357/ab5fdd](https://doi.org/10.3847/1538-4357/ab5fdd) (2020). [1912.05206](https://arxiv.org/abs/1912.05206).
16. Narayanan, D., Conroy, C., Davé, R., Johnson, B. D. & Popping, G. A Theory for the Variation of Dust Attenuation Laws in Galaxies. *ApJ* **869**, 70, DOI: [10.3847/1538-4357/aaed25](https://doi.org/10.3847/1538-4357/aaed25) (2018). [1805.06905](https://arxiv.org/abs/1805.06905).
17. Trayford, J. W., Lagos, C. d. P., Robotham, A. S. G. & Obreschkow, D. Fade to grey: systematic variation of galaxy attenuation curves with galaxy properties in the EAGLE simulations. *MNRAS* **491**, 3937–3951, DOI: [10.1093/mnras/stz3234](https://doi.org/10.1093/mnras/stz3234) (2020). [1908.08956](https://arxiv.org/abs/1908.08956).
18. Ferrara, A., Bianchi, S., Cimatti, A. & Giovanardi, C. An Atlas of Monte Carlo Models of Dust Extinction in Galaxies for Cosmological Applications. *ApJS* **123**, 437–445, DOI: [10.1086/313244](https://doi.org/10.1086/313244) (1999). [astro-ph/9903078](https://arxiv.org/abs/astro-ph/9903078).
19. Boquien, M. *et al.* The ALPINE-ALMA [C II] survey. Dust attenuation curves at $z = 4.4\text{--}5.5$. *A@AND@A* **663**, A50, DOI: [10.1051/0004-6361/202142537](https://doi.org/10.1051/0004-6361/202142537) (2022). [2202.11723](https://arxiv.org/abs/2202.11723).
20. Markov, V. *et al.* Dust attenuation law in JWST galaxies at $z \sim 7\text{--}8$. *A@AND@A* **679**, A12, DOI: [10.1051/0004-6361/202346723](https://doi.org/10.1051/0004-6361/202346723) (2023).
21. Witstok, J. *et al.* Carbonaceous dust grains seen in the first billion years of cosmic time. *Nature* **621**, 267–270, DOI: [10.1038/s41586-023-06413-w](https://doi.org/10.1038/s41586-023-06413-w) (2023). [2302.05468](https://arxiv.org/abs/2302.05468).
22. Gallerani, S. *et al.* The extinction law at high redshift and its implications. *A@AND@A* **523**, A85, DOI: [10.1051/0004-6361/201014721](https://doi.org/10.1051/0004-6361/201014721) (2010). [1006.4463](https://arxiv.org/abs/1006.4463).
23. Di Mascia, F. *et al.* The dust attenuation law in $z \sim 6$ quasars. *MNRAS* **506**, 3946–3961, DOI: [10.1093/mnras/stab1876](https://doi.org/10.1093/mnras/stab1876) (2021). [2106.15625](https://arxiv.org/abs/2106.15625).
24. Stratta, G., Gallerani, S. & Maiolino, R. Is GRB 050904 at $z = 6.3$ absorbed by dust? *A@AND@A* **532**, A45, DOI: [10.1051/0004-6361/201016414](https://doi.org/10.1051/0004-6361/201016414) (2011). [1106.4441](https://arxiv.org/abs/1106.4441).
25. Bolmer, J. *et al.* Dust reddening and extinction curves toward gamma-ray bursts at $z > 4$. *A@AND@A* **609**, A62, DOI: [10.1051/0004-6361/201731255](https://doi.org/10.1051/0004-6361/201731255) (2018). [1709.06867](https://arxiv.org/abs/1709.06867).
26. Calzetti, D. *et al.* The Dust Content and Opacity of Actively Star-forming Galaxies. *ApJ* **533**, 682–695, DOI: [10.1086/308692](https://doi.org/10.1086/308692) (2000). [astro-ph/9911459](https://arxiv.org/abs/astro-ph/9911459).

27. Gordon, K. D., Clayton, G. C., Misselt, K. A., Landolt, A. U. & Wolff, M. J. A Quantitative Comparison of the Small Magellanic Cloud, Large Magellanic Cloud, and Milky Way Ultraviolet to Near-Infrared Extinction Curves. *ApJ* **594**, 279–293, DOI: [10.1086/376774](https://doi.org/10.1086/376774) (2003). [astro-ph/0305257](https://arxiv.org/abs/astro-ph/0305257).
28. Cardelli, J. A., Clayton, G. C. & Mathis, J. S. The Relationship between Infrared, Optical, and Ultraviolet Extinction. *ApJ* **345**, 245, DOI: [10.1086/167900](https://doi.org/10.1086/167900) (1989).
29. Boyer, M. L. *et al.* An Infrared Census of DUST in Nearby Galaxies with Spitzer (DUSTINGS). IV. Discovery of High-redshift AGB Analogs. *ApJ* **851**, 152, DOI: [10.3847/1538-4357/aa9892](https://doi.org/10.3847/1538-4357/aa9892) (2017). [1711.02129](https://arxiv.org/abs/1711.02129).
30. Burgarella, D. *et al.* Observational and theoretical constraints on the formation and early evolution of the first dust grains in galaxies at $5 < z < 10$. *A&A* **637**, A32, DOI: [10.1051/0004-6361/201937143](https://doi.org/10.1051/0004-6361/201937143) (2020). [2002.01858](https://arxiv.org/abs/2002.01858).
31. Spitzer, L. *Physical processes in the interstellar medium* (1978).
32. Dwek, E. & Scalo, J. M. The evolution of refractory interstellar grains in the solar neighborhood. *ApJ* **239**, 193–211, DOI: [10.1086/158100](https://doi.org/10.1086/158100) (1980).
33. Ferrara, A. *et al.* A physical model for [C II] line emission from galaxies. *MNRAS* **489**, 1–12, DOI: [10.1093/mnras/stz2031](https://doi.org/10.1093/mnras/stz2031) (2019). [1908.07536](https://arxiv.org/abs/1908.07536).
34. Pallottini, A. *et al.* Deep into the structure of the first galaxies: SERRA views. *MNRAS* **487**, 1689–1708, DOI: [10.1093/mnras/stz1383](https://doi.org/10.1093/mnras/stz1383) (2019). [1905.08254](https://arxiv.org/abs/1905.08254).
35. Pallottini, A. *et al.* A survey of high- z galaxies: SERRA simulations. *MNRAS* **513**, 5621–5641, DOI: [10.1093/mnras/stac1281](https://doi.org/10.1093/mnras/stac1281) (2022). [2201.02636](https://arxiv.org/abs/2201.02636).
36. Vallini, L., Ferrara, A., Pallottini, A., Carniani, S. & Gallerani, S. Star formation law in the epoch of reionization from [C II] and C III] lines. *MNRAS* **495**, L22–L26, DOI: [10.1093/mnras/slaa047](https://doi.org/10.1093/mnras/slaa047) (2020). [2003.06443](https://arxiv.org/abs/2003.06443).
37. Markov, V. *et al.* The interstellar medium of high-redshift galaxies: Gathering clues from C III] and [C II] lines. *A&A* **663**, A172, DOI: [10.1051/0004-6361/202243336](https://doi.org/10.1051/0004-6361/202243336) (2022). [2206.03503](https://arxiv.org/abs/2206.03503).
38. Förster Schreiber, N. M. *et al.* The SINS Survey: SINFONI Integral Field Spectroscopy of $z \sim 2$ Star-forming Galaxies. *ApJ* **706**, 1364–1428, DOI: [10.1088/0004-637X/706/2/1364](https://doi.org/10.1088/0004-637X/706/2/1364) (2009). [0903.1872](https://arxiv.org/abs/0903.1872).
39. Meštrić, U. *et al.* Exploring the physical properties of lensed star-forming clumps at $2 \lesssim z \lesssim 6$. *MNRAS* **516**, 3532–3555, DOI: [10.1093/mnras/stac2309](https://doi.org/10.1093/mnras/stac2309) (2022). [2202.09377](https://arxiv.org/abs/2202.09377).
40. Ferrara, A., Pallottini, A. & Dayal, P. On the stunning abundance of super-early, luminous galaxies revealed by JWST. *MNRAS* **522**, 3986–3991, DOI: [10.1093/mnras/stad1095](https://doi.org/10.1093/mnras/stad1095) (2023). [2208.00720](https://arxiv.org/abs/2208.00720).
41. Pallottini, A. & Ferrara, A. Stochastic star formation in early galaxies: Implications for the James Webb Space Telescope. *A&A* **677**, L4, DOI: [10.1051/0004-6361/202347384](https://doi.org/10.1051/0004-6361/202347384) (2023). [2307.03219](https://arxiv.org/abs/2307.03219).
42. Behrens, C., Pallottini, A., Ferrara, A., Gallerani, S. & Vallini, L. Dusty galaxies in the Epoch of Reionization: simulations. *MNRAS* **477**, 552–565, DOI: [10.1093/mnras/sty552](https://doi.org/10.1093/mnras/sty552) (2018). [1802.07772](https://arxiv.org/abs/1802.07772).
43. Carniani, S. *et al.* Kiloparsec-scale gaseous clumps and star formation at $z = 5-7$. *MNRAS* **478**, 1170–1184, DOI: [10.1093/mnras/sty1088](https://doi.org/10.1093/mnras/sty1088) (2018). [1712.03985](https://arxiv.org/abs/1712.03985).
44. Markov, V. *et al.* Massive molecular gas reservoir around the central AGN in the CARLA J1103 + 3449 cluster at $z = 1.44$. *A&A* **641**, A22, DOI: [10.1051/0004-6361/202038673](https://doi.org/10.1051/0004-6361/202038673) (2020). [2007.03706](https://arxiv.org/abs/2007.03706).
45. Sommovigo, L. *et al.* A new look at the infrared properties of $z \sim 5$ galaxies. *MNRAS* **517**, 5930–5941, DOI: [10.1093/mnras/stac2997](https://doi.org/10.1093/mnras/stac2997) (2022). [2210.09312](https://arxiv.org/abs/2210.09312).
46. Carnall, A. C., McLure, R. J., Dunlop, J. S. & Davé, R. Inferring the star formation histories of massive quiescent galaxies with BAGPIPES: evidence for multiple quenching mechanisms. *MNRAS* **480**, 4379–4401, DOI: [10.1093/mnras/sty2169](https://doi.org/10.1093/mnras/sty2169) (2018). [1712.04452](https://arxiv.org/abs/1712.04452).
47. Buat, V. *et al.* GOODS-Herschel: evidence of a UV extinction bump in galaxies at $z > 1$. *A&A* **533**, A93, DOI: [10.1051/0004-6361/201117264](https://doi.org/10.1051/0004-6361/201117264) (2011). [1107.1049](https://arxiv.org/abs/1107.1049).
48. Buat, V. *et al.* GOODS-Herschel: dust attenuation properties of UV selected high redshift galaxies. *A&A* **545**, A141, DOI: [10.1051/0004-6361/201219405](https://doi.org/10.1051/0004-6361/201219405) (2012). [1207.3528](https://arxiv.org/abs/1207.3528).
49. Kriek, M. & Conroy, C. The Dust Attenuation Law in Distant Galaxies: Evidence for Variation with Spectral Type. *ApJL* **775**, L16, DOI: [10.1088/2041-8205/775/1/L16](https://doi.org/10.1088/2041-8205/775/1/L16) (2013). [1308.1099](https://arxiv.org/abs/1308.1099).

50. Scoville, N. *et al.* Dust Attenuation in High Redshift Galaxies: “Diamonds in the Sky”. *ApJ* **800**, 108, DOI: [10.1088/0004-637X/800/2/108](https://doi.org/10.1088/0004-637X/800/2/108) (2015). [1412.8219](https://arxiv.org/abs/1412.8219).
51. Reddy, N. A. *et al.* The MOSDEF Survey: Measurements of Balmer Decrements and the Dust Attenuation Curve at Redshifts $z \sim 1.4$ – 2.6 . *ApJ* **806**, 259, DOI: [10.1088/0004-637X/806/2/259](https://doi.org/10.1088/0004-637X/806/2/259) (2015). [1504.02782](https://arxiv.org/abs/1504.02782).
52. Tress, M. *et al.* SHARDS: constraints on the dust attenuation law of star-forming galaxies at $z \sim 2$. *MNRAS* **475**, 2363–2374, DOI: [10.1093/mnras/stx3334](https://doi.org/10.1093/mnras/stx3334) (2018). [1801.01128](https://arxiv.org/abs/1801.01128).
53. Shivaiei, I. *et al.* The MOSDEF Survey: The Variation of the Dust Attenuation Curve with Metallicity. *ApJ* **899**, 117, DOI: [10.3847/1538-4357/aba35e](https://doi.org/10.3847/1538-4357/aba35e) (2020). [2005.01742](https://arxiv.org/abs/2005.01742).
54. Li, A. *et al.* On Dust Extinction of Gamma-Ray Burst Host Galaxies. *ApJ* **685**, 1046–1051, DOI: [10.1086/591049](https://doi.org/10.1086/591049) (2008). [0808.4115](https://arxiv.org/abs/0808.4115).
55. Noll, S. *et al.* GMASS ultra-deep spectroscopy of galaxies at $z \sim 2$. IV. The variety of dust populations. *A&A* **499**, 69–85, DOI: [10.1051/0004-6361/200811526](https://doi.org/10.1051/0004-6361/200811526) (2009). [0903.3972](https://arxiv.org/abs/0903.3972).
56. Salmon, B. *et al.* Breaking the Curve with CANDELS: A Bayesian Approach to Reveal the Non-Universality of the Dust-Attenuation Law at High Redshift. *ApJ* **827**, 20, DOI: [10.3847/0004-637X/827/1/20](https://doi.org/10.3847/0004-637X/827/1/20) (2016). [1512.05396](https://arxiv.org/abs/1512.05396).
57. Hsu, Y.-M., Hirashita, H., Lin, Y.-H., Camps, P. & Baes, M. Effects of dust sources on dust attenuation properties in IllustrisTNG galaxies at $z \sim 7$. *MNRAS* **519**, 2475–2485, DOI: [10.1093/mnras/stac3666](https://doi.org/10.1093/mnras/stac3666) (2023). [2212.04759](https://arxiv.org/abs/2212.04759).
58. Charlot, S. & Fall, S. M. A Simple Model for the Absorption of Starlight by Dust in Galaxies. *ApJ* **539**, 718–731, DOI: [10.1086/309250](https://doi.org/10.1086/309250) (2000). [astro-ph/0003128](https://arxiv.org/abs/astro-ph/0003128).
59. Zanella, A. *et al.* A contribution of star-forming clumps and accreting satellites to the mass assembly of $z \sim 2$ galaxies. *MNRAS* **489**, 2792–2818, DOI: [10.1093/mnras/stz2099](https://doi.org/10.1093/mnras/stz2099) (2019). [1907.12136](https://arxiv.org/abs/1907.12136).
60. McKinnon, R., Vogelsberger, M., Torrey, P., Marinacci, F. & Kannan, R. Simulating galactic dust grain evolution on a moving mesh. *MNRAS* **478**, 2851–2886, DOI: [10.1093/mnras/sty1248](https://doi.org/10.1093/mnras/sty1248) (2018). [1805.04521](https://arxiv.org/abs/1805.04521).
61. Hirashita, H. & Murga, M. S. Self-consistent modelling of aromatic dust species and extinction curves in galaxy evolution. *MNRAS* **492**, 3779–3793, DOI: [10.1093/mnras/stz3640](https://doi.org/10.1093/mnras/stz3640) (2020). [2001.01968](https://arxiv.org/abs/2001.01968).
62. Makiya, R. & Hirashita, H. Cosmic evolution of grain size distribution in galaxies using the v^2GC semi-analytical model. *MNRAS* **517**, 2076–2087, DOI: [10.1093/mnras/stac2762](https://doi.org/10.1093/mnras/stac2762) (2022). [2210.06176](https://arxiv.org/abs/2210.06176).
63. Nozawa, T. *et al.* Evolution of Dust in Primordial Supernova Remnants: Can Dust Grains Formed in the Ejecta Survive and Be Injected into the Early Interstellar Medium? *ApJ* **666**, 955–966, DOI: [10.1086/520621](https://doi.org/10.1086/520621) (2007). [0706.0383](https://arxiv.org/abs/0706.0383).
64. Asano, R. S., Takeuchi, T. T., Hirashita, H. & Nozawa, T. What determines the grain size distribution in galaxies? *MNRAS* **432**, 637–652, DOI: [10.1093/mnras/stt506](https://doi.org/10.1093/mnras/stt506) (2013). [1303.5528](https://arxiv.org/abs/1303.5528).
65. Tazaki, R. & Ichikawa, K. Dust Destruction by Drift-induced Sputtering in Active Galactic Nuclei. *ApJ* **892**, 149, DOI: [10.3847/1538-4357/ab72f6](https://doi.org/10.3847/1538-4357/ab72f6) (2020). [2002.01736](https://arxiv.org/abs/2002.01736).
66. Tazaki, R., Ichikawa, K. & Kokubo, M. Dust Destruction by Charging: A Possible Origin of Gray Extinction Curves of Active Galactic Nuclei. *ApJ* **892**, 84, DOI: [10.3847/1538-4357/ab7822](https://doi.org/10.3847/1538-4357/ab7822) (2020). [2002.08023](https://arxiv.org/abs/2002.08023).
67. Winters, J. M., Fleischer, A. J., Le Bertre, T. & Sedlmayr, E. Circumstellar dust shells around long-period variables. V. A consistent time-dependent model for the extreme carbon star AFGL 3068. *A&A* **326**, 305–317 (1997).
68. Ferrarotti, A. S. & Gail, H. P. Composition and quantities of dust produced by AGB-stars and returned to the interstellar medium. *A&A* **447**, 553–576, DOI: [10.1051/0004-6361:20041198](https://doi.org/10.1051/0004-6361:20041198) (2006).
69. Leńniewska, A. & Michałowski, M. J. Dust production scenarios in galaxies at $z \sim 6$ – 8.3 . *A&A* **624**, L13, DOI: [10.1051/0004-6361/201935149](https://doi.org/10.1051/0004-6361/201935149) (2019). [1904.11185](https://arxiv.org/abs/1904.11185).
70. Maiolino, R. *et al.* A supernova origin for dust in a high-redshift quasar. *Nature* **431**, 533–535, DOI: [10.1038/nature02930](https://doi.org/10.1038/nature02930) (2004). [astro-ph/0409577](https://arxiv.org/abs/astro-ph/0409577).
71. Brammer, G. [grizli](https://arxiv.org/abs/2301.00000) (2023).
72. Brammer, G. [msaexp: NIRSpec analysis tools](https://arxiv.org/abs/2205.00000), DOI: [10.5281/zenodo.7299500](https://doi.org/10.5281/zenodo.7299500) (2022).
73. Jwst user documentation. <https://jwst-docs.stsci.edu/jwst-near-infrared-spectrograph/nirspec-operations/nirspec-mos-operations/nirspec-mos-operations-slit-losses> (2017).

74. Beck, T. L. *et al.* Planning JWST NIRSpec MSA spectroscopy using NIRCам pre-images. In Peck, A. B., Seaman, R. L. & Benn, C. R. (eds.) *Observatory Operations: Strategies, Processes, and Systems VI*, vol. 9910 of *Society of Photo-Optical Instrumentation Engineers (SPIE) Conference Series*, 99101O, DOI: [10.1117/12.2232804](https://doi.org/10.1117/12.2232804) (2016).
75. Chevallard, J. & Charlot, S. Modelling and interpreting spectral energy distributions of galaxies with beagle. *Mon. Notices Royal Astron. Soc.* **462**, 1415–1443, DOI: [10.1093/mnras/stw1756](https://doi.org/10.1093/mnras/stw1756) (2016). <https://academic.oup.com/mnras/article-pdf/462/2/1415/8011909/stw1756.pdf>.
76. Ferland, G. J. *et al.* The 2017 Release Cloudy. *Revista Mexicana de Astron.* **53**, 385–438, DOI: [10.48550/arXiv.1705.10877](https://doi.org/10.48550/arXiv.1705.10877) (2017). [1705.10877](https://arxiv.org/abs/1705.10877).
77. Inoue, A. K., Shimizu, I., Iwata, I. & Tanaka, M. An updated analytic model for attenuation by the intergalactic medium. *MNRAS* **442**, 1805–1820, DOI: [10.1093/mnras/stu936](https://doi.org/10.1093/mnras/stu936) (2014). [1402.0677](https://arxiv.org/abs/1402.0677).
78. Leja, J., Carnall, A. C., Johnson, B. D., Conroy, C. & Speagle, J. S. How to Measure Galaxy Star Formation Histories. II. Nonparametric Models. *ApJ* **876**, 3, DOI: [10.3847/1538-4357/ab133c](https://doi.org/10.3847/1538-4357/ab133c) (2019). [1811.03637](https://arxiv.org/abs/1811.03637).
79. Topping, M. W. *et al.* The ALMA REBELS Survey: specific star formation rates in the reionization era. *MNRAS* **516**, 975–991, DOI: [10.1093/mnras/stac2291](https://doi.org/10.1093/mnras/stac2291) (2022). [2203.07392](https://arxiv.org/abs/2203.07392).
80. Salim, S., Boquien, M. & Lee, J. C. Dust Attenuation Curves in the Local Universe: Demographics and New Laws for Star-forming Galaxies and High-redshift Analogs. *ApJ* **859**, 11, DOI: [10.3847/1538-4357/aabf3c](https://doi.org/10.3847/1538-4357/aabf3c) (2018). [1804.05850](https://arxiv.org/abs/1804.05850).
81. Feroz, F., Hobson, M. P., Cameron, E. & Pettitt, A. N. Importance Nested Sampling and the MultiNest Algorithm. *The Open J. Astrophys.* **2**, 10, DOI: [10.21105/astro.1306.2144](https://doi.org/10.21105/astro.1306.2144) (2019). [1306.2144](https://arxiv.org/abs/1306.2144).
82. Viaene, S. *et al.* The Herschel Exploitation of Local Galaxy Andromeda (HELGA). VII. A SKIRT radiative transfer model and insights on dust heating. *A@AND@A* **599**, A64, DOI: [10.1051/0004-6361/201629251](https://doi.org/10.1051/0004-6361/201629251) (2017). [1609.08643](https://arxiv.org/abs/1609.08643).
83. Williams, T. G. *et al.* High-resolution radiative transfer modelling of M33. *MNRAS* **487**, 2753–2770, DOI: [10.1093/mnras/stz1441](https://doi.org/10.1093/mnras/stz1441) (2019). [1905.09838](https://arxiv.org/abs/1905.09838).
84. De Looze, I. *et al.* High-resolution, 3D radiative transfer modeling. I. The grand-design spiral galaxy M 51. *A@AND@A* **571**, A69, DOI: [10.1051/0004-6361/201424747](https://doi.org/10.1051/0004-6361/201424747) (2014). [1409.3857](https://arxiv.org/abs/1409.3857).
85. Declair, M. *et al.* Revealing the dust attenuation properties on resolved scales in NGC 628 with SWIFT UVOT data. *MNRAS* **486**, 743–767, DOI: [10.1093/mnras/stz805](https://doi.org/10.1093/mnras/stz805) (2019). [1903.06715](https://arxiv.org/abs/1903.06715).
86. Burgarella, D., Buat, V. & Iglesias-Páramo, J. Star formation and dust attenuation properties in galaxies from a statistical ultraviolet-to-far-infrared analysis. *MNRAS* **360**, 1413–1425, DOI: [10.1111/j.1365-2966.2005.09131.x](https://doi.org/10.1111/j.1365-2966.2005.09131.x) (2005). [astro-ph/0504434](https://arxiv.org/abs/astro-ph/0504434).
87. Conroy, C., Schiminovich, D. & Blanton, M. R. Dust Attenuation in Disk-dominated Galaxies: Evidence for the 2175 Å Dust Feature. *ApJ* **718**, 184–198, DOI: [10.1088/0004-637X/718/1/184](https://doi.org/10.1088/0004-637X/718/1/184) (2010). [1003.2202](https://arxiv.org/abs/1003.2202).
88. Wild, V. *et al.* Empirical determination of the shape of dust attenuation curves in star-forming galaxies. *MNRAS* **417**, 1760–1786, DOI: [10.1111/j.1365-2966.2011.19367.x](https://doi.org/10.1111/j.1365-2966.2011.19367.x) (2011). [1106.1646](https://arxiv.org/abs/1106.1646).
89. Battisti, A. J., Calzetti, D. & Chary, R. R. Characterizing Dust Attenuation in Local Star-forming Galaxies: UV and Optical Reddening. *ApJ* **818**, 13, DOI: [10.3847/0004-637X/818/1/13](https://doi.org/10.3847/0004-637X/818/1/13) (2016). [1601.00208](https://arxiv.org/abs/1601.00208).
90. Declair, M. *DustKING - Revealing the dust attenuation in nearby galaxies*. Ph.D. thesis, Ghent University, Belgium (2019).
91. Jakobsen, P. *et al.* The Near-Infrared Spectrograph (NIRSpec) on the James Webb Space Telescope. I. Overview of the instrument and its capabilities. *A@AND@A* **661**, A80, DOI: [10.1051/0004-6361/202142663](https://doi.org/10.1051/0004-6361/202142663) (2022). [2202.03305](https://arxiv.org/abs/2202.03305).
92. Bunker, A. J. *et al.* JADES NIRSpec Initial Data Release for the Hubble Ultra Deep Field: Redshifts and Line Fluxes of Distant Galaxies from the Deepest JWST Cycle 1 NIRSpec Multi-Object Spectroscopy. *arXiv e-prints* arXiv:2306.02467, DOI: [10.48550/arXiv.2306.02467](https://doi.org/10.48550/arXiv.2306.02467) (2023). [2306.02467](https://arxiv.org/abs/2306.02467).

Methods

Spectroscopic data

We use publicly available Near Infrared Spectrograph (NIRSpec) data retrieved from the DAWN JWST Archive (DJA)⁶, an initiative of the Cosmic Dawn Center. DJA includes all publicly available Cycle 1 and 2 spectroscopic and photometric observations from various JWST surveys. The data reduction was performed entirely and uniformly with GRIZLI (Grism redshift and line analysis software for space-based slitless spectroscopy⁷¹) and MSAEXP (Tool for extracting JWST NIRSpec Micro-Shutter Assembly (MSA) spectra⁷²) Python scripts, by the Cosmic Dawn Center.

Here, we focus on the analysis of NIRSpec prism spectra. The output 1D spectra achieve wavelength-dependent resolution of $R \sim 30 - 300$, ranging from $\lambda \sim 0.6 - 5.3 \mu\text{m}$. This allows us to probe the nebular lines and continuum emission from rest-frame UV to IR. However, due to the limited velocity resolution of $\gtrsim 1000 \text{ km s}^{-1}$, we are unable to resolve nebular emission lines. A fraction of the spectral region below the wavelength of the Ly α line is selectively masked due to the potential contamination by the intervening neutral IGM.

Sample selection

Our target selection process closely follows the one outlined in our recent work²⁰. We conduct a visual inspection of all grade 3¹ NIRSpec prism spectra, opting for galaxies exhibiting a prominent continuum and nebular line emission while excluding sources with strong negative features.

We select sources at $z > 2$ to ensure that we can effectively probe the rest-frame UV-optical wavelength range, allowing us to accurately constrain the shape of the dust attenuation curve and the potential presence of the UV bump. We further clean our sample by selecting spectra with an average channel Signal-to-Noise (S/N) ratio of $S/N > 3$, in the rest-frame wavelength range of 1925 – 2425 Å, corresponding to the peak position of the UV bump (2175 Å). Additionally, we conduct a visual examination of the spectral energy distribution (SED) fits for all sources observed with NIRSpec. Any objects for which the SED models cannot yield a reasonable fit within the associated uncertainties are excluded from further consideration.

Finally, we exclude galaxies that exhibit negligible dust attenuation (i.e., with $A_V \sim 0$) from our initial sample. For a galaxy to be considered "dusty", it must meet two criteria: (1) V -band dust attenuation of $A_V > 0.1$; (2) $A_V > 0$ with a $\sigma > 3$.

Slit-loss correction

The flux values at a given wavelength reported in JWST NIRSpec micro-shutter assembly (MSA)-based data may not always coincide with the ones reported in photometric data. The discrepancy between the NIRSpec MSA spectra and the photometric data can arise from several factors such as slit-losses, flux calibration of both spectra and photometry, and spectroscopic and photometric aperture. Slit-loss refers to the reduction in the observed flux in spectroscopic data due to extension and off-centred location of the science target in the NIRSpec spectrograph shutters of finite dimensions ($0.20'' \times 0.46''$)^{73,74}. The impact of slit-loss is wavelength-dependent since the full width at half maximum (FWHM) of the point spread function (PSF) widens with increasing wavelength.

To address the impact of slit-loss and correct for the discrepancy between the NIRSpec spectra and the photometric data, we employ the following approach. First, we utilise the Python tool by DJA⁶ to extract photometry from *Hubble* Space Telescope (HST), JWST Near-Infrared Camera (NIRCAM), and JWST Near-Infrared Imager and Slitless Spectrograph (NIRISS), using the right ascension, declination and redshift for each target. Next, we overlay the photometric points onto the spectrum for comparison. If needed, we correct the spectrum by dividing it with one of the throughputs provided by the JWST user documentation⁷³, until achieving a satisfactory alignment between the spectra and photometry.

Galaxy sample

We ended up with a final sample of 173 "dusty" galaxies. These galaxies fall within a spectroscopic redshift range of $2.0 \lesssim z \lesssim 11.4$, (with a median redshift of $z \approx 4.6$), with stellar masses of $6.9 \lesssim \log M_*/M_\odot \lesssim 10.9$, star formation rates $0.1 \lesssim \text{SFR}/M_\odot \text{ yr}^{-1} \lesssim 240$ and V -band dust attenuation $0.1 \lesssim A_V \lesssim 2.3$.

Fig. 3 depicts a large diversity of attenuation curves of our full JWST sample. For instance, the slopes range from those shallower than the Calzetti curve to the ones considerably steeper than the SMC curve. The strength of the UV bump varies considerably from curves in which it is completely absent (as in the SMC case) to those surpassing the bump strength observed in the MW. In Fig. 3 we also plot the median attenuation curve along with its 1σ uncertainties, computed from the full JWST sample. The median curve and its uncertainties are derived from the 16th, 50th, and 84th percentiles of a set of 5000 attenuation curves that are generated using a bootstrapping approach, which involves 5000 random sampling of the $c_1 - c_4$ parameters constrained for the entire galaxy sample.

¹Grade 3 is given to spectra in which the spectroscopic redshift is confidently determined by relying on robust spectroscopic features.

SED fitting

In our recent study²⁰, we presented a customized version of the `BAGPIPES` SED fitting code⁴⁶ that enables us to simultaneously constrain the fundamental physical properties of galaxies (e.g. SFR, M_* , Z) and the shape of their dust attenuation law. In this section, we give a summary of our method.

`BAGPIPES` is a Bayesian SED fitting code that generates realistic galaxy spectra using the Stellar Population Synthesis (SPS) models⁷⁵, nebular emission models pre-computed with `CLOUDY` photoionization code⁷⁶, and InterGalactic Medium (IGM) models⁷⁷. The Star Formation History (SFH) can be parameterized with various parametric and flexible SFH models. We employ the non-parametric SFH model with a "continuity" prior as our fiducial SFH model, since it allows greater flexibility in fitting the "true" SFHs and constraining less biased physical properties of galaxies, compared to parametric models^{20,78,79}.

The warm dust emission component within HII regions is included in `CLOUDY`, whereas the cold dust emission component within the neutral ISM is modelled with the grey body emission. The dust attenuation recipe includes a two-component dust screen model⁵⁸ to account for extra attenuation toward the stellar birth clouds. Dust attenuation can be modelled using standard empirical templates: "Calzetti"²⁶ attenuation curve, SMC²⁷ and MW extinction curves²⁸ and flexible dust models^{58,80}. We implement the analytical dust attenuation law⁵⁴ into `BAGPIPES` and we use it as our fiducial dust attenuation model. The analytical form of the dust attenuation law, normalised by A_V is:

$$A_\lambda/A_V = \frac{c_1}{(\lambda/0.08)^{c_2} + (0.08/\lambda)^{c_2} + c_3} + \frac{233[1 - c_1/(6.88^{c_2} + 0.145^{c_2} + c_3) - c_4/4.60]}{(\lambda/0.046)^2 + (0.046/\lambda)^2 + 90} + \frac{c_4}{(\lambda/0.2175)^2 + (0.2175/\lambda)^2 - 1.95}, \quad (1)$$

where c_1, \dots, c_4 are dimensionless parameters and λ is the wavelength in μm . The three components of the Drude model describe the rise in far ultraviolet (FUV) attenuation, attenuation within the optical and near-infrared (NIR) spectrum, and the 2175 Å bump, respectively. The main advantage of this flexible dust model is its capability to replicate local empirical dust curves (Calzetti, MW, SMC) and to recover any potential variations in the dust attenuation laws of early galaxies.

`BAGPIPES` is based on a Bayesian approach and the MultiNest nested sampling algorithm⁸¹. `BAGPIPES` requires to provide the instructions on the SED model, that is, the parameters of the model components (e.g., SFH, nebular emission, and dust attenuation) and their priors. In this work, the selected prior probability densities for model parameters are nearly identical to those of our initial work²⁰. However, the allowed prior limits have been expanded to encompass a potentially wider parameter space that could be relevant for a larger galaxy sample spanning a significantly broader redshift range of $z \sim 2 - 12$. For instance, prior limits are set to allow super-solar metallicities (up to $Z \sim 2.5 Z_\odot$), high dust content ($A_V \sim 8$, and prominent UV bump ($c_4 \sim 0.1$). The prior probability distributions for each of the parameters of the model are given in Table 1.

Attenuation curve parametrization

To compare our constrained dust attenuation curves with those documented in the literature, we employ the parameterization introduced by Salim & Narayanan (2020)⁴. The primary parameters of their work that provide information about the wavelength-dependent attenuation characteristics are the UV-optical slope (S) and UV bump strength (B)⁴. The slope S is defined as $S = A_{1500}/A_V$, where A_{1500} is attenuation at $\lambda = 1500 \text{ \AA}$ and A_V is the attenuation in the V -band (i.e., at $\lambda = 5500 \text{ \AA}$).

The UV bump strength, B is defined as $B = A_{\text{bump}}/A_{2175}$, where A_{bump} refers to the extra attenuation attributed to the bump above the baseline at $\lambda = 2175 \text{ \AA}$, and A_{2175} is the total attenuation at $\lambda = 2175 \text{ \AA}$. We note that in the original parametrization of the UV bump with the B parameter⁴, the baseline at 2175 Å is calculated using a relation derived from simulated attenuation curves¹⁶ $A_{2175,0} = 0.33A_{1500} + 0.67A_{A3000}$. In this work, we derive the 2175 Å baseline by fitting the dust curve with an analytical dust model⁵⁴ and setting the c_4 parameter (which serves as a proxy for the UV bump strength) as $c_4 = 0$. This approach allows us to constrain the UV bump parameter B more precisely, with slightly reduced uncertainties.

Comparison with the literature

In Fig. 2 we report the literature findings for the slope S and the bump B . The MW²⁸ and the SMC²⁷ are indicated by blue dotted lines. Other local individual sources: M31⁸², M33⁸³, M51⁸⁴, and M74⁸⁵ are depicted as blue circles. The median/mean values of samples of nearby ($z \sim 0$) and intermediate- z ($z \sim 1 - 4$) galaxies from various studies^{26,47-51,53,86-90} are represented by green circles. Slopes for subsamples of low and intermediate- z galaxies are shown as magenta⁸⁰ and cyan⁵² circles, respectively. Finally, individual high- z ($z \sim 4 - 8$) sources are indicated by violet¹⁹ and orange circles²⁰.

Literature results for all the local sources and most nearby^{26,86-89} and intermediate- z ⁴⁷⁻⁵¹ galaxy samples are directly adopted from the work of Salim & Narayanan (2020)⁴. Specific literature values of S and B are recalculated from their original

parametrizations using the relations provided by Salim & Narayanan (2020)⁴. For instance, certain studies⁸⁰ utilize the Charot & Fall (2000) parametrization⁵⁸, $A_\lambda/A_V = (\lambda/0.55\mu m)^{-n}$, where the power law exponent n characterizes the UV-optical slope. In such cases, we make use of the relation $\log S = n/1.772$ to convert to the S parameter. In works that use the Noll et al. (2009) parametrization^{55,90}, and the δ parameter to parametrize the slope, we use the relation $\log S = 0.4 - 0.55\delta$. Tress et al. (2018)⁵² use the Conroy et al. (2010) parametrization⁸⁷ and they provide a relation to convert to the Noll et al. (2009) parametrization⁵⁵. Finally, the remaining literature results^{20,53,90} are directly provided by the authors.

To date, the detection of the characteristic 2175 Å feature has been reported in two galaxies at $z \sim 7$ ^{20,21}, both of which are also a part of the DAWN sample. Witstok et al. (2023)²¹ reported a UV bump detection (with a $\sigma \sim 4$) in the JADES-GS-z6-0 galaxy, achieved by fitting an excess attenuation at 2175 Å with a Drude profile. However, applying our method to the full spectrum of JADES-GS-z6-0 from DAWN resulted in a non-detection, with a UV bump strength of $B = 0.239 \pm 0.213$ or $c_4 = 0.032^{+0.038}_{-0.027}$. In our recent study²⁰, we reported a hint of a UV bump detection in one out of three high- z sources, s00717 at $z \sim 6.9$, with a UV bump strength of $c_4 = 0.033^{+0.013}_{-0.012}$ ($\sigma \sim 2.7$). Employing the identical SED fitting method with the same set of priors²⁰ on the DAWN observations of the s00717 source yields $c_4 = 0.019^{+0.031}_{-0.017}$. Inconsistencies in these results may arise from the use of different data reduction pipelines generating slightly different final 1D spectra. For s00717 the data reduction was performed with the standard pipeline⁹¹, whereas JADES-GS-z6-0 was reduced by a custom version of the pipeline⁹². The data in this work are reduced with the MSAEXP custom code⁷². The different pipeline versions have different sampling, resulting in slightly different flux densities, uncertainties, and channel widths, which can create inconsistencies (for s00717 and JADES-GS-z6-0), as well as various fitting procedures involving different models (for JADES-GS-z6-0). When investigating the redshift evolution of galaxy properties, it is thus recommended to adopt samples of galaxies for which the data reduction analysis is performed with the same pipeline, as in the case of our study.

Observational and model uncertainties

Factors that could contribute to the discrepancy in slopes between our study and the ones from the literature at $z \sim 2$ can arise both from observational uncertainties and model dependencies. Regarding the observational uncertainties, at the low redshift limit of our sample ($z \sim 2 - 2.8$), NIRSpec prism observations ($\lambda \sim 0.6 - 5.3 \mu m$) are restricted to the rest-frame $\lambda \gtrsim 1600 - 2000 \text{ \AA}$, which probe the UV bump peak and marginally extend into the far-UV rise of the attenuation curve. This constraint in wavelength coverage may contribute to larger uncertainties in inferred slopes. Moreover, for $z \sim 2 - 2.8$ sources, NIRSpec data are probing the attenuation curve with a fraction of the spectra at shorter wavelengths, which suffer from larger uncertainties, due to the lower resolution ($R \sim \lambda/\Delta\lambda \sim 50$) of the NIRSpec prism disperser in the wavelength range of $\lambda_{\text{obs}} \sim 0.5 - 2 \mu m^2$.

Regarding the model dependencies, different SED fitting codes with different sets of model prescriptions and imposed priors on parameters^{48,52} can have a significant impact on the output parameters, including the recovered attenuation curve.

Acknowledgements

We would like to express our gratitude to H. Hirashita and I. Shivaeei for engaging in productive discussions with us and providing valuable insights and comments. Additionally, we thank to M. Declair and I. Shivaeei for sharing their findings on the attenuation curve properties. VM, AF, and AP acknowledge support from the ERC Advanced Grant INTERSTELLAR H2020/740120. Partial support (AF) from the Carl Friedrich von Siemens-Forschungspreis der Alexander von Humboldt-Stiftung Research Award is kindly acknowledged. Any dissemination of results must indicate that it reflects only the author’s view and that the Commission is not responsible for any use that may be made of the information it contains. The data products presented herein were retrieved from the Dawn JWST Archive (DJA). DJA is an initiative of the Cosmic Dawn Center, which is funded by the Danish National Research Foundation under grant No. 140. We gratefully acknowledge the computational resources of the Center for High Performance Computing (CHPC) at SNS.

Author contributions

VM, SG, and AF led the writing of this paper. EP, VM, MK, and SG contributed to the target selection. VM, EP, and SG contributed to the visual inspection and additional data reduction. SG, VM, and AP contributed to the sample cleaning. VM led the SED fitting of the selected targets. SG, VM, AF, AP, LS, and FDM contributed to the development of the customized SED fitting tool. VM, SG, LS, AP, AF, and MK contributed to the visualisation of the results. VM, SG, AP, MK, AF, EP, and FDM contributed to the analysis of the results. VM, AF, SG, and AP contributed to the discussion on the physical interpretation of the results. All authors reviewed the manuscript.

²<https://jwst-docs.stsci.edu/jwst-near-infrared-spectrograph/nirspec-instrumentation/nirspec-dispersers-and-filters>

Competing interests

The authors declare no competing interests.

Additional information

Data availability The data that support the findings of this study are available at <https://dawn-cph.github.io/dja/index.html>.

Accession codes GRIZLI (Grism redshift and line analysis software for space-based slitless spectroscopy⁷¹) and MSAEXP (Tool for extracting JWST NIRSpec Micro-Shutter Assembly (MSA) spectra⁷², and BAGPIPES (Bayesian Analysis of Galaxies for Physical Inference and Parameter Estimation)⁴⁶ Python scripts are publicly available at <https://github.com/gbrammer/grizli>, <https://github.com/gbrammer/msaexp>, and <https://github.com/ACCarnall/bagpipes>, respectively.

Correspondence and requests for materials should be addressed to Vladan Markov, Simona Gallerani, or Andrea Ferrara.

Extended data

Table 1. SED fitting parameters and their priors.

Parameter	Limits	Prior
Global		
z	$(z_{\text{sp}} - 0.5, z_{\text{sp}} + 0.5)$	Uniform
$\sigma_v/\text{km s}^{-1}$	$(1, 2000)$	Logarithmic
SFH		
$\log M_*^{\text{form}}/M_\odot$	$(4, 13)$	Uniform
Z/Z_\odot	$(0.001, 2.5)$	Logarithmic
$\Delta \log(\text{SFR})_i$	$(-10, 10)$	Student's-t
nebular emission		
$\log U$	$(-4, 0)$	Uniform
dust		
A_V/mag	$(0, 8)$	Uniform
c_1	$(0, 75)$	Uniform
c_2	$(2, 20)$	Uniform
c_3	$(-2, 75)$	Uniform
c_4	$(-0.005, 0.1)$	Uniform

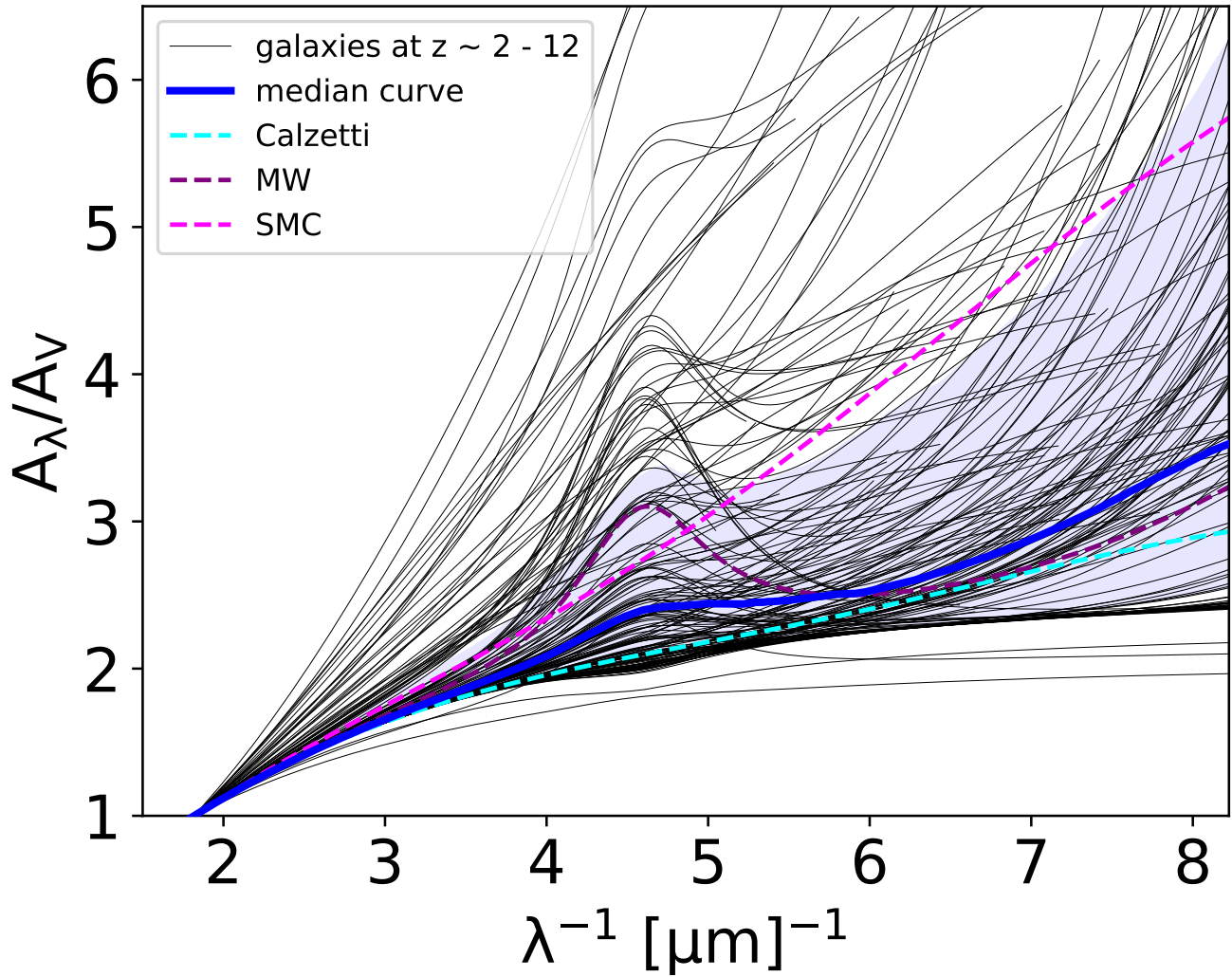


Figure 3. Dust attenuation curves of our full sample of JWST galaxies at $z \sim 2 - 12$, derived using our SED fitting method. The median curve along with its 1σ uncertainties is depicted as a blue solid line with a corresponding shaded region. The Calzetti, the MW, and the SMC, empirical curves are shown as cyan, purple, and magenta dashed lines, respectively.

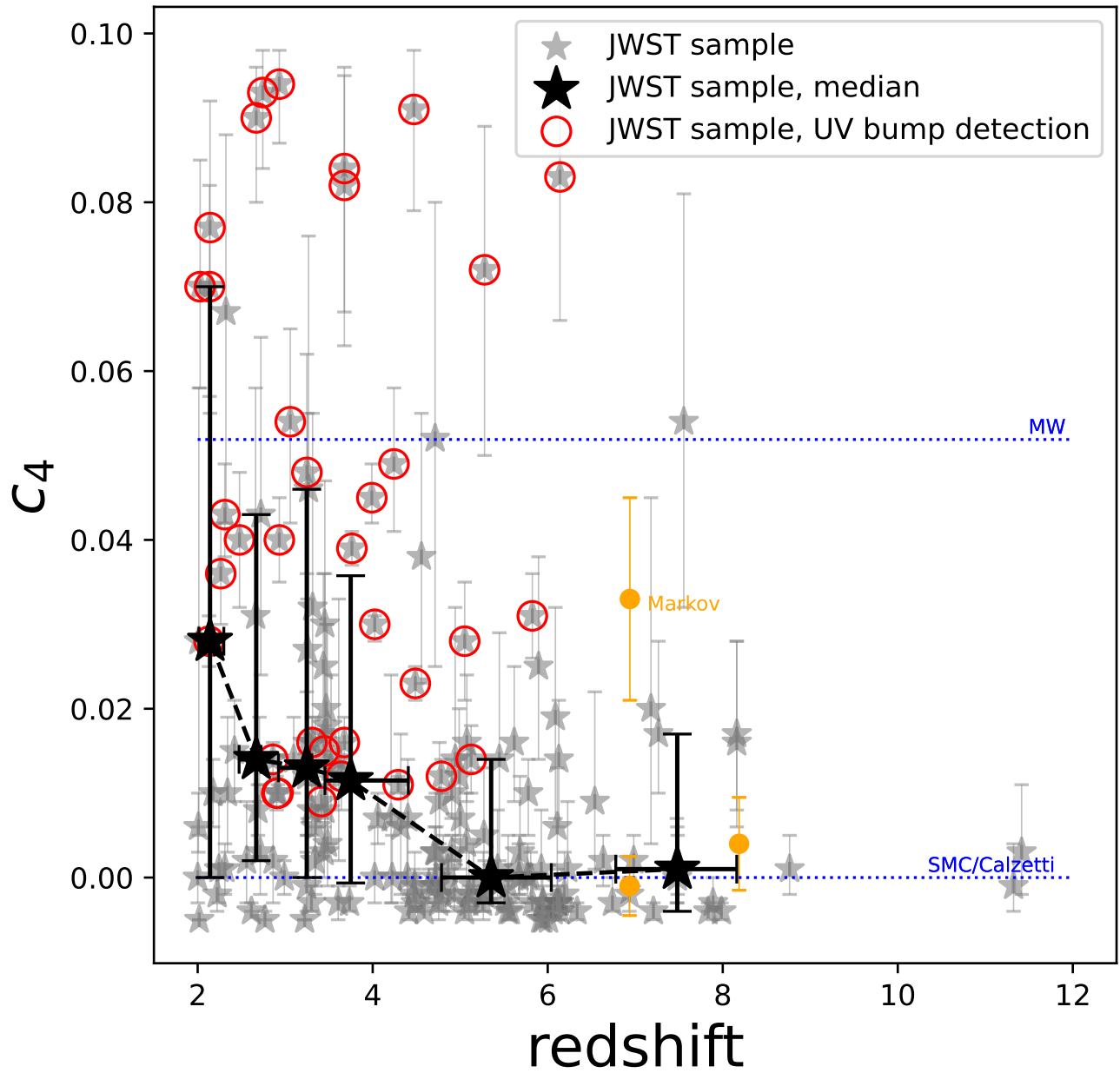


Figure 4. UV bump strength, parametrized by the c_4 parameter⁵⁴, as a function of redshift. Our entire JWST galaxy sample is represented by grey stars. Among these, those with UV bump detection are highlighted with a red circle. The median c_4 values for subsamples of galaxies binned by redshift (corresponding to the redshift bins of Fig. 1) are indicated by black stars. Symbols are the same as in Fig. 2.

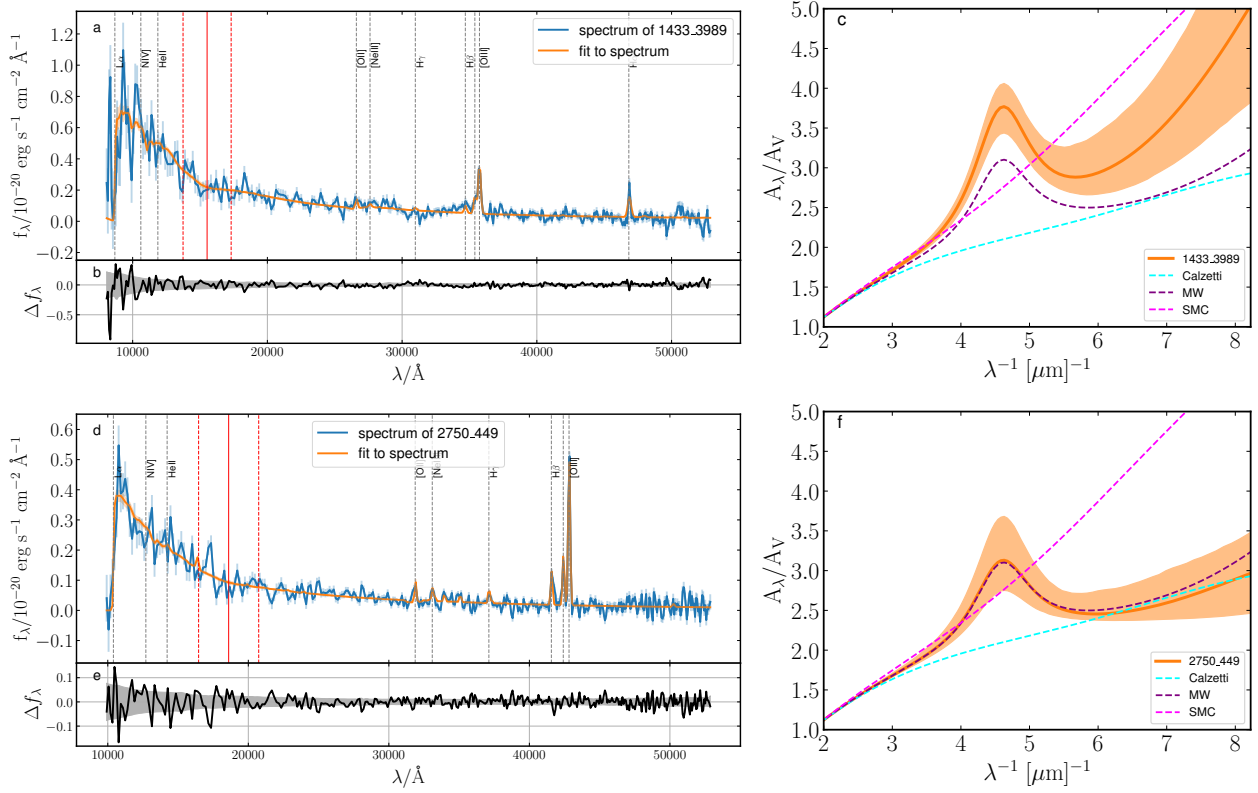


Figure 5. SED fitting results for two high-redshift sources exhibiting UV-bump detection. Top row (panels a - c): SED fit for the 1433_3989 galaxy at $z \approx 6.14$. Bottom row (panels d - f): SED fit for 2750_449 at $z \approx 7.55$. **a, d**, The NIRSpect *JWST* spectrum and the best-fit posterior, along with their corresponding 1σ uncertainties are indicated in blue and orange, respectively. Vertical grey and red lines mark the positions of potential emission lines and the UV bump absorption feature of the spectrum. **b, e**, Residuals of the best fit on the observed spectrum, Δf_λ , with 1σ uncertainties. **c, f**, The best-fit dust attenuation curve with 1σ uncertainties. Dust model fits to the Calzetti, the MW, and the SMC empirical curves are depicted as cyan, purple, and magenta dashed lines, respectively.